Experimental study of the $3\,^1\Delta_g$ and $4\,^1\Delta_g$ states of the Rb_2 molecule

J. T. Stahovich,[1] B. A. Rowe,[1] P. T. Arndt,[1] A. D. Hersh,[1] P. L. Wardach,[1] J. P. Huennekens,[2] V. B. Sovkov,[3,4] A. M. Lyyra,[1] and E. H. Ahmed[1,*]

[1]*Department of Physics, Temple University, Philadelphia, Pennsylvania 19122, USA*
[2]*Department of Physics, Lehigh University, Bethlehem, Pennsylvania 18015, USA*
[3]*St. Petersburg State University, 7/9 Universitetskaya naberezhnaya, St. Petersburg 199034, Russia*
[4]*State Key Laboratory of Quantum Optics and Quantum Optics Devices, Institute of Laser spectroscopy, College of Physics and Electronics, Shanxi University, Taiyuan 030006, China*

(Received 2 October 2023; accepted 4 December 2023; published 10 January 2024)

We report an experimental study of the highly excited $3\,^1\Delta_g$ and $4\,^1\Delta_g$ electronic states of the Rb_2 molecule. Rovibrational levels of the two electronic states were probed using the high-resolution optical-optical double resonance technique by exciting $^{85}Rb_2$ molecules from thermally populated levels of the $X\,^1\Sigma_g^+$ ground state through intermediate levels of the $B\,^1\Pi_u$ electronic state. The $^1\Delta_g$ resonances induced by the probe laser were observed by detecting laser induced fluorescence from collisionally populated triplet states lying near the upper $^1\Delta_g$ states to the $a\,^3\Sigma_u^+$ triplet ground state. The $^1\Delta_g$ character of the two electronic states was confirmed by showing that the probe transitions to these states abide by $^1\Delta \leftarrow {}^1\Pi$ dipole selection rules and by observing that their lowest rotational level is $J = 2$. A set of molecular constants and a Rydberg-Klein-Rees potential-energy curve were calculated from the observed term values for each electronic state and compared with *ab initio* predictions.

DOI: 10.1103/PhysRevA.109.012805

I. INTRODUCTION

Alkali-metal atoms and their diatomic molecules have relatively simple hydrogen-atom-like and hydrogen-molecule-like electronic structures. This comparative simplicity, coupled with convenient transition wavelengths in the visible and near-IR, has made them the system of choice for a wide range of atomic, molecular, and optical physics experiments. The electronic structure of alkali-metal atoms is well known with very high accuracy from numerous experimental studies [1]. In contrast, the structure of alkali-metal dimers is less well studied. However, with the rapid development of applications and methods for creation of ultracold molecules [2–10] there is substantial need for additional spectroscopic studies of the alkali dimers. This is the case specifically for the highly excited states of the heavier Rb_2 and Cs_2 alkali dimers for which systematic experimental explorations are hindered by the high density of states, as well as by the presence of strong perturbations. Nevertheless, highly excited states with *ungerade* symmetry have been studied experimentally using polarization labeling [11–13] and resonance enhanced two-photon ionization [14] spectroscopy. In both techniques, the excited electronic states are probed by direct single laser excitation of ground $X\,^1\Sigma_g^+$ state molecules. Since selection rules do not allow transitions between electronic states with the same parity of the electronic wave-function inversion operator $\hat{i}$, to study highly excited electronic states with *gerade* symmetry a different approach is needed. In our recent spectroscopic studies of the Rb_2 molecule we showed that excited singlet [15,16] and triplet [17] states with *gerade* symmetry originating from the $5s + 6p$ and $5p + 5p$ atomic limits can be explored using the optical-optical double resonance (OODR) and perturbation facilitated OODR (PFOODR) techniques [18–20]. In the present work, we extend this approach to higher energies by observing experimentally the highly excited $3^1\Delta_g$ and $4^1\Delta_g$ states originating from the $5s + 5d$ and $5s + 4f$ atomic limits, respectively. We report experimentally determined Dunham coefficients and RKR potential energy curves for these two states.

II. EXPERIMENT

The experimental setup used in this work is the same as described previously [17]. Rubidium metal (Alfa Aesar 10315, 99.75%) with a natural isotopic abundance ratio of ^{85}Rb and ^{87}Rb [21] was placed inside a five arm, stainless steel heat-pipe oven [22]. Using electric heaters, the oven center was heated to a temperature of 180° C, producing $\sim 1.39 \times 10^{-2}$ Torr of atomic rubidium and the three isotopologues ($^{85}Rb_2$, $^{85}Rb^{87}Rb$, and $^{87}Rb_2$) of the rubidium molecule at a total molecular pressure of approximately 1.8×10^{-5} Torr [23]. To contain the rubidium vapor to the center of the heat pipe and keep it from condensing on the windows, argon at pressure of 1.4 Torr, measured at room temperature, was used as a buffer gas in conjunction with chilled water lines wrapped around the ends of the heat-pipe oven arms.

The present work concentrated on the energy levels of the $3^1\Delta_g$ and $4^1\Delta_g$ states of the Rb_2 molecule. The excitation scheme used in the experiment is illustrated in Fig. 1. To minimize the residual Doppler linewidth, the pump and probe lasers were in a counterpropagating configuration [24–28].

*Corresponding author: erahmed@temple.edu

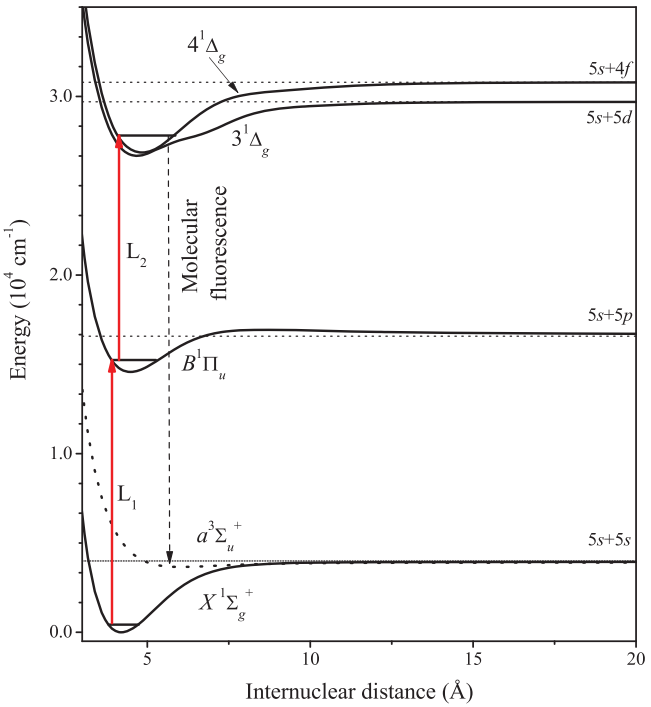

FIG. 1. The excitation scheme used in the experiment and the relevant potential-energy curves of the rubidium dimer molecule. The pump laser L_1 selectively excites molecules from one of the thermally populated rovibrational levels of the $X\,^1\Sigma_g^+$ ground state to an intermediate rovibrational level of the $B^1\Pi_u$ state. Then, the probe laser L_2 further excites these molecules to rovibrational levels of the target $3^1\Delta_g$ and $4^1\Delta_g$ states. The probe laser resonances are detected by monitoring fluorescence to the $a^3\Sigma_u^+$ triplet ground state from collisionally populated triplet states lying near the upper $^1\Delta_g$ states. The potential-energy curves used in this figure are the *ab initio* calculations from Ref. [13].

The pump transition was driven by a tunable, continuous-wave (cw) Coherent 699-29 ring dye laser, operating with DCM dye. This laser selectively excites molecules from a thermally populated rovibrational level of the ground $X\,^1\Sigma_g^+$ electronic state [29] to a suitable intermediate level in the well-known $B^1\Pi_u$ state [30]. With the pump laser fixed to a $B \leftarrow X$ transition, population was further excited to the high lying $3^1\Delta_g$ and $4^1\Delta_g$ target states by scanning a tunable, cw Coherent 899-29 ring Ti:sapphire laser. The pump and probe lasers were calibrated using an iodine cell [31,32] and a uranium hollow cathode lamp [33,34], respectively.

The probe laser transitions to the $^1\Delta_g$ states were observed by detecting laser induced fluorescence (LIF) from nearby collisionally-populated triplet states [35–37] to the $a^3\Sigma_u^+$ triplet ground state [38], using a photomultiplier tube (PMT, R928P Hamamatsu Photonics) with blue-light band-pass filters (Kopp Glass 5543 and 5562). The PMT housing and glass filter assembly were attached directly to one of the arms of the heat-pipe oven. The PMT output was amplified using a lock-in amplifier (SR850 Stanford Research) while the pump laser beam was modulated at a frequency of 1 kHz using a rotating chopper (SR540 Stanford Research). The amplified signal was recorded as a function of the probe laser frequency. To determine the probe laser resonances that originated from the target $B^1\Pi_u(v', J')$ intermediate level, each probe scan was recorded twice; once with the pump laser tuned to a P branch, $B^1\Pi_u(v', J') \leftarrow X\,^1\Sigma_g^+(v'', J'' = J' + 1)$, and once with it tuned to an R branch, $B^1\Pi_u(v', J') \leftarrow X\,^1\Sigma_g^+(v'', J'' = J' - 1)$. Only probe resonances observed at the same probe frequency and with similar intensity and line shape were considered as originating from the specific $B^1\Pi_u(v', J')$ level of interest. In addition, in the process of determining the Λ quantum number of the observed states, a few vibrational Q branch, $B^1\Pi_u(v', J') \leftarrow X\,^1\Sigma_g^+(v'', J'' = J')$, pump transitions were also employed. We label the vibrational levels with the letter v and for the angular momenta and their projections on the internuclear axis we follow the standard notations [39]; $\vec{L}$ is the total electron orbital angular momentum with projection Λ, $\vec{S}$ is the total electron spin with projection Σ, $\vec{R}$ is the nuclear rotational angular momentum, and $\vec{J} = \vec{L} + \vec{S} + \vec{R}$ is the total angular momentum of the system, exclusive of nuclear spin, with projection $\Omega = \Lambda + \Sigma$.

III. ANALYSIS AND RESULTS

Utilizing the OODR configuration illustrated in Fig. 1, we were able to observe rovibrational levels of two electronic states in the energy region $26650 - 27750\,\mathrm{cm}^{-1}$ above the bottom of the Rb_2 ground state potential-energy curve. From the $B^1\Pi_u$ intermediate level, only direct excitations to $^1\Sigma_g^{+/-}$, $^1\Pi_g$ and $^1\Delta_g$ states are electric dipole allowed [39–41]. We have observed in the probe laser scans that each vibrational transition contains P, Q, and R rotational branches of similar intensity [see Fig. 2(a)]. Since transitions with $\Delta\Lambda = 0$ exhibit rapidly decreasing Q branch intensity with increasing rotational quantum number, we can rule out the possibility that the upper states are of $^1\Pi_g$ character. Furthermore, $^1\Sigma_g^{+/-}$ character for these states can be ruled out based on the e/f parity selection rules, i.e., $e \leftrightarrow e$ and $f \leftrightarrow f$ for P and R branch transitions, and $e \leftrightarrow f$ for Q branch transitions. This is because all rovibrational levels of the ground $X\,^1\Sigma_g^+$ state have e parity. Thus, P and R pump transitions only populate e parity components of the $B^1\Pi_u$ intermediate levels, whereas Q branch pump transitions only populate f parity components of the $B^1\Pi_u$ intermediate levels. Similarly, rotational levels of upper $^1\Sigma_g^+$ or $^1\Sigma_g^-$ states all have only e parity or only f parity, respectively. Thus, even though P, Q, and R branches are allowed, in principle, for $^1\Sigma \leftarrow {}^1\Pi$ electronic transitions, the P and R branches must originate from one parity level of the $B^1\Pi_u$ state, while Q transitions must originate from the other parity level of $B^1\Pi_u$. In our experiment, only one of the e/f parity components of the intermediate level is populated in each pump/probe configuration. Therefore, if the upper state is either $^1\Sigma_g^+$ or $^1\Sigma_g^-$, we would observe either P and R rotational branches (with no Q branch), or only a Q branch (with no P or R branches) in our probe laser scans. In contrast, for $^1\Delta \leftarrow {}^1\Pi$ probe transitions P, Q, and R branch transitions are all allowed. Since each rotational level of a $^1\Delta$ state has both e and f parity components, all three branches will be observed in the probe laser excitations from either e

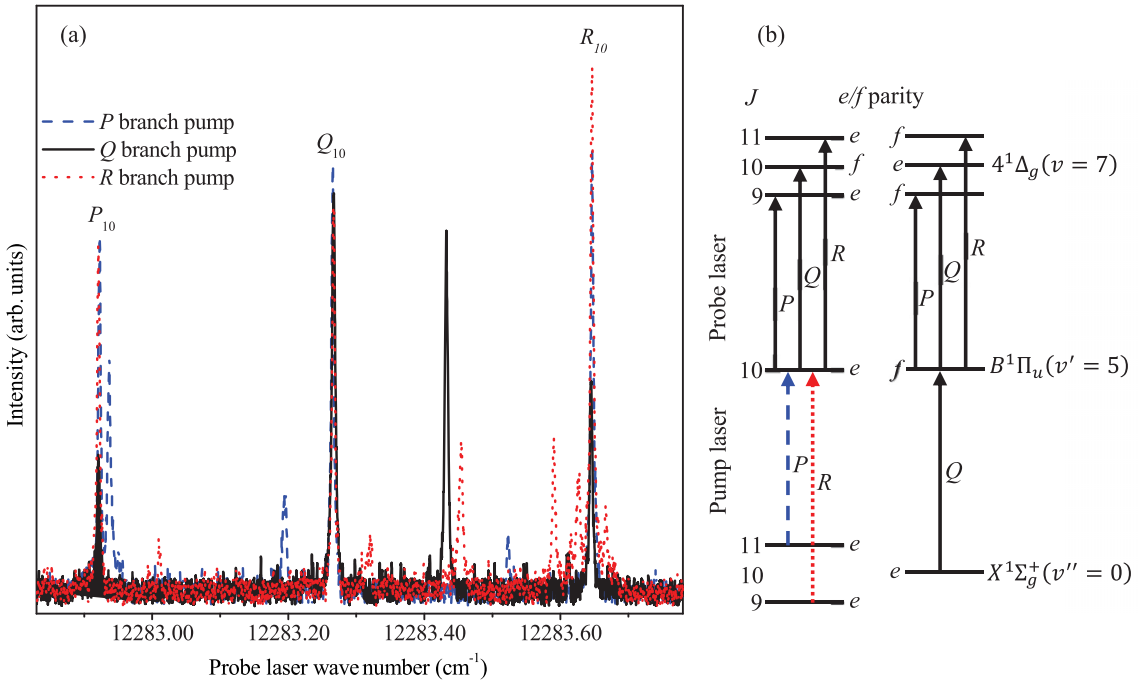

FIG. 2. (a) A set of LIF probe laser scans containing the confirmed P_{10}, Q_{10}, and R_{10} rotational branches for the $4^1\Delta_g(v=7) \leftarrow B^1\Pi_u(v'=5)$ vibrational transition with pump laser set on the P_{11} (blue dashes), Q_{10} (black), and R_9 (red dots) rotational branches of the $B^1\Pi_u(v'=5) \leftarrow X\,^1\Sigma_g^+(v''=0)$ vibrational transition. (b) Illustration of the possible OODR excitation pathways and rotational parity of the levels involved.

or f parity components of the $B^1\Pi_u$ state, as is illustrated in Fig. 2(b). Furthermore, since $\Lambda = 2$ for a $^1\Delta$ state, the lowest rotational levels ($R = 0$) have a total electronic angular momentum quantum number of $J = 2$. We have confirmed this experimentally for the observed states by recording a set of probe laser scans for a specific vibrational level of each state from the lowest three rotational levels ($J' = 3,\ 2,$ and 1) of the $B^1\Pi_u$ state (see Fig. 3). For both states, all three rotational branches are observed in the probe spectrum when a pump transition to a $J' = 3$ level of the intermediate state is used [Fig. 3(a)]. However, when the pump laser excites molecules to a $J' = 2$ level of the $B^1\Pi_u$ state, the P_2 branch is missing [Fig. 3(b)], and only the R_1 branch is observed in the probe spectrum when a $J' = 1$ level of the $B^1\Pi_u$ intermediate state is utilized [Fig. 3(c)]. The lack of P_2, P_1, and Q_1 branches in the observed spectra in Fig. 3 indicates that the lowest rotational levels of the excited target states have an angular momentum quantum number of $J = 2$. Thus, based on the electronic and rotational transition selection rules for diatomic molecules [39–41], the two observed states were identified as $^1\Delta_g$ states.

In addition, we have calculated the relative intensities of the individual rotational branches in the probe laser excitation spectra to compare to experiment. In this work, the efficiency of the fluorescence detection system is only very weakly dependent on polarization, and since the upper state of the detected triplet band fluorescence is populated by collisions, we do not expect the fluorescence to be strongly polarized in any case. Under these conditions, it is fair to assume that the fluorescence signal, measured for a particular choice of pump and probe laser transitions, $[^1\Delta_g(v,J) \leftarrow B^1\Pi_u(v',J') \leftarrow X^1\Sigma_g^+(v'',J'')]$, is proportional to the upper level population $N[^1\Delta(v,J)]$; i.e.,

$$\text{Signal} \propto N[^1\Delta_g(v,J)] = \sum_M N[^1\Delta_g(v,J,M)], \qquad (1)$$

where in the last step we sum over the populations in the individual M sublevels. Because we use vertically polarized pump and probe laser light for excitation, we can take the vertical direction to be the quantization axis, and note that both the pump and probe lasers can only induce $\Delta M = 0$ transitions. Thus, the M levels are uncoupled and no interference effects occur (i.e., there is only one path to each upper M level).

We can calculate the relative upper M level populations from the initial (ground state) M'' level populations and the relevant dipole matrix elements $|\langle\hat{\varepsilon}_I \cdot \vec{\mu}\rangle|$. Following Lefebvre-Brion and Field [41], Sec. 6.3.2, using a space fixed coordinate system (XYZ) and with a laser polarization vector $\hat{I}$, we can write

$$\hat{\varepsilon}_I \cdot \vec{\mu} = \mu_I = \tfrac{1}{2}\alpha_I^+\mu^- + \tfrac{1}{2}\alpha_I^-\mu^+ + \alpha_I^z\mu_z,$$

where $\hat{\varepsilon}_I$ is the (space fixed) laser polarization vector and the $\alpha_I^j \equiv \hat{I} \cdot \hat{j}$ are direction cosine operator components linking unit vectors in the space fixed (XYZ) and body fixed (xyz) coordinate systems, $\alpha_I^\pm = \alpha_I^x \pm i\alpha_I^y$ and $\mu^\pm = \mp\frac{1}{\sqrt{2}}(\mu_x \pm i\mu_y)$. Here $I = Z$, so $\hat{\varepsilon}_I = \hat{\varepsilon}_Z$ and $\hat{\varepsilon}_I \cdot \vec{\mu} = \hat{\varepsilon}_Z \cdot \vec{\mu} = \mu_Z = \tfrac{1}{2}\alpha_Z^+\mu^- + \tfrac{1}{2}\alpha_Z^-\mu^+ + \alpha_Z^z\mu_z$. This expression allows us to factor dipole matrix elements into electronic-transition-specific, molecule-fixed, nonrotating molecule matrix elements of μ_j times rotating molecule matrix elements of α_Z^j.

Writing the molecular wave functions as products $|\Omega JM\rangle|n\Lambda S\Sigma\rangle$, where n specifies the electronic state and vibrational level, S is the electronic spin, Σ and Λ are projections of electron spin and electron orbital angular momenta onto the internuclear axis, $\Omega = \Lambda + \Sigma$, and M is the component of the nuclear rotation J along the laboratory fixed Z axis, it can be shown that for $\Delta\Omega = 0$ transitions

$$\begin{aligned}&\langle n_f(\Lambda_f = \Lambda_i)S\Sigma|\langle(\Omega_f = \Omega_i)J_fM_f|\mu_I|\Omega_iJ_iM_i\rangle|n_i\Lambda_iS\Sigma\rangle \\ &\quad = \langle n_f\Lambda_iS\Sigma|\langle\Omega_iJ_fM_f|\alpha_I^z\mu_z|\Omega_iJ_iM_i\rangle|n_i\Lambda_iS\Sigma\rangle = \mu_\parallel[n_f\Lambda_i, n_i\Lambda_i]\langle\Omega_iJ_fM_f|\alpha_I^z|\Omega_iJ_iM_i\rangle,\end{aligned} \tag{2}$$

while for $\Delta\Omega = \pm1$ transitions (where both states are not $\Sigma_{\Omega=0}$ states)

$$\begin{aligned}&\langle n_f(\Lambda_f = \Lambda_i \pm 1)S\Sigma|\langle(\Omega_f = \Omega_i \pm 1)J_fM_f|\mu_I|\Omega_iJ_iM_i\rangle|n_i\Lambda_iS\Sigma\rangle = \langle n_f(\Lambda_i \pm 1)S\Sigma|\langle(\Omega_i \pm 1)J_fM_f|\tfrac{1}{2}\alpha_I^\mp\mu^\pm|\Omega_iJ_iM_i\rangle|n_i\Lambda_iS\Sigma\rangle \\ &\quad = \frac{1}{\sqrt{2}}\mu_\perp[n_f(\Lambda_i \pm 1), n_i\Lambda_i]\langle(\Omega_i \pm 1)J_fM_f|\alpha_I^\mp|\Omega_iJ_iM_i\rangle.\end{aligned} \tag{3}$$

Here we have used the fact that dipole transitions only couple states of the same S and Σ; i.e., that $S_f = S_i \equiv S$ and $\Sigma_f = \Sigma_i \equiv \Sigma$. (Note that Σ here represents the projection of $\vec{S}$ onto the molecular axis, and should not be confused with a Σ state where $\Lambda = 0$.) In these expressions, we label the initial and final states with subscripts i and f, respectively. In addition, $\mu_\parallel[n_f\Lambda_i, n_i\Lambda_i] \equiv \langle n_f\Lambda_i|\mu_z|n_i\Lambda_i\rangle$ always and $\mu_\perp[n_f(\Lambda_i \pm 1), n_i\Lambda_i] \equiv \frac{1}{\sqrt{2}}\langle n_f(\Lambda_i \pm 1)|\mu^\pm|n_i\Lambda_i\rangle$ for $\Lambda_i,\ \Lambda_f > 0$. Using e/f symmetrized basis functions $\frac{1}{\sqrt{2}}\{|\Omega JM\rangle|n\Lambda S\Sigma\rangle \pm |-\Omega JM\rangle|n, -\Lambda, S, -\Sigma\rangle\}$, Lefebvre-Brion and Field show that the factor of $\frac{1}{\sqrt{2}}$ in Eq. (3) does not appear for $\Sigma_{\Omega=0} \to \Pi$ or $\Pi \to \Sigma_{\Omega=0}$ transitions. Symmetrized basis functions must be used because the real e and f energy levels are eigenvalues of these symmetrized eigenstates.

Applying these results, we find

$$\langle\hat{\varepsilon}_I \cdot \vec{\mu}\rangle = \mu_\parallel[n_f\Lambda_i, n_i\Lambda_i]\langle\Omega_iJ_fM_f|\alpha_I^z|\Omega_iJ_iM_i\rangle \tag{4}$$

for $\Delta\Lambda = \Delta\Omega = 0$ transitions. For $\Delta\Lambda = \Delta\Omega = \pm1$ transitions with $\Lambda_i,\ \Lambda_f > 0$ (i.e., $\Pi \to \Delta$ transitions)

$$\langle\hat{\varepsilon}_I \cdot \vec{\mu}\rangle = \frac{1}{\sqrt{2}}\mu_\perp[n_f(\Lambda_i \pm 1), n_i\Lambda_i]\langle(\Omega_i \pm 1)J_fM_f|\alpha_I^\mp|\Omega_iJ_iM_i\rangle, \tag{5}$$

and for $\Delta\Lambda = \Delta\Omega = \pm1$ transitions with either $\Lambda_i = 0$ or $\Lambda_f = 0$ (i.e., $\Sigma_{\Omega=0} \to \Pi$ or $\Pi \to \Sigma_{\Omega=0}$ transitions)

$$\langle\hat{\varepsilon}_I \cdot \vec{\mu}\rangle = \mu_\perp[n_f(\Lambda_i \pm 1), n_i\Lambda_i]\langle(\Omega_i \pm 1)J_fM_f|\alpha_I^\mp|\Omega_iJ_iM_i\rangle. \tag{6}$$

In the present case, $\hat{\varepsilon}_I = \hat{\varepsilon}_Z$, and we are dealing with a $^1\Pi \leftarrow {}^1\Sigma$ transition and a $^1\Delta \leftarrow {}^1\Pi$ transition. Both are $\Delta\Lambda = \Delta\Omega = +1$ transitions. Thus, the matrix elements we need are

$$\langle\hat{\varepsilon}_Z \cdot \vec{\mu}\rangle = \mu_\perp[n'(\Lambda'' + 1), n''\Lambda'']\langle(\Omega'' + 1)J'(M' = M'')|\alpha_Z^-|\Omega''J''M''\rangle$$

with $\Lambda'' = \Omega'' = 0$ for the $^1\Pi \leftarrow {}^1\Sigma$ pump transition, and

$$\langle\hat{\varepsilon}_Z \cdot \vec{\mu}\rangle = \frac{1}{\sqrt{2}}\mu_\perp[n(\Lambda' + 1), n'\Lambda']\langle(\Omega' + 1)J(M = M' = M'')|\alpha_Z^-|\Omega'J'(M' = M'')\rangle$$

with $\Lambda' = \Omega' = 1$ for the $^1\Delta \leftarrow {}^1\Pi$ probe transition.

The upper state population in sublevel M is proportional to the initial (ground state) M'' level population multiplied by the squares of the pump and probe transition dipole matrix elements. Hence the measured signal is given by

$$\begin{aligned}\text{Signal} &\propto \sum_M N[^1\Delta_g(v, J, M)] \\ &\propto \sum_{M''}\left\{N[X\,^1\Sigma_g^+(v'', J'', M'')].|\mu_\perp[B^1\Pi_u, X\,^1\Sigma_g^+]\langle(\Omega'' + 1)J'(M' = M'')|\alpha_Z^-|\Omega''J''M''\rangle|^2\right. \\ &\quad \left.\times\frac{1}{2}.|\mu_\perp[^1\Delta_g, B^1\Pi_u]\langle(\Omega' + 1)J(M = M' = M'')|\alpha_Z^-|\Omega'J'(M' = M'')\rangle|^2\right\} \\ &\propto \frac{1}{2}|\mu_\perp[B^1\Pi_u, X\,^1\Sigma_g^+]|^2|\mu_\perp[^1\Delta_g, B^1\Pi_u]|^2\sum_{M''}\{N[X\,^1\Sigma_g^+(v'', J'', M'')] \\ &\quad \times|\langle(\Omega'' + 1)J'(M' = M'')|\alpha_Z^-|\Omega''J''M''\rangle|^2|\langle(\Omega' + 1)J(M = M' = M'')|\alpha_Z^-|\Omega'J'(M' = M'')\rangle|^2\}.\end{aligned} \tag{7}$$

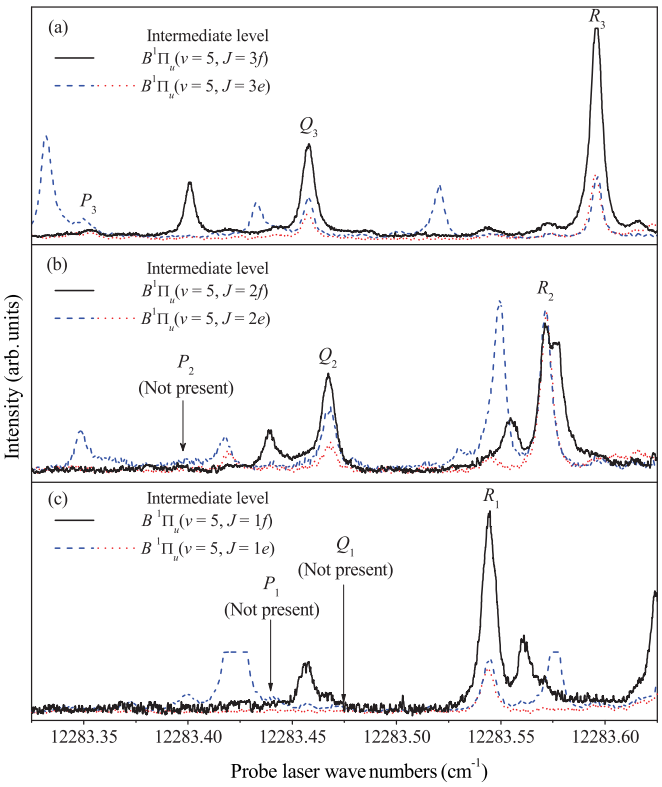

FIG. 3. LIF probe laser scans for the $4^1\Delta_g(v=7) \leftarrow B^1\Pi_u(v'=5)$ vibrational transition with rotational levels of $J'=3$ (a), $J'=2$ (b), and $J'=1$ (c) for the $B^1\Pi_u$ intermediate state. In each figure, spectra with the Q branch rotational pump transition, $B^1\Pi_u(v'=5, J') \leftarrow X\,^1\Sigma_g^+(v''=0,\ J''=J')$, are indicated with the black trace, while P and R branch rotational pump transitions, $B^1\Pi_u(v'=5, J') \leftarrow X\,^1\Sigma_g^+(v''=0,\ J''=J'\pm 1)$, are indicated with blue dashed and red dotted traces, respectively. Transitions that only appear in one of the three spectra in a given panel, such as the blue peak at the far left of panel (a), are associated with other intermediate state levels that happen to be simultaneously populated at the same pump laser frequency. Arrows indicate the positions of the missing P_1, Q_1, and P_2 lines. We note that transitions to the $3^1\Delta_g$ state display the same patterns.

The $\mu_\perp$ terms only depend on the electronic and vibrational states and thus do not affect the relative intensities of the rotational transitions. Similarly, we assume that the ground state M'' levels are equally populated initially. Thus the intensities of the rotational level signals depend entirely on the matrix elements $\langle(\Omega''+1)J'(M'=M'')|\alpha_Z^-|\Omega''J''M''\rangle$ and $\langle(\Omega'+1)J(M=M'=M'')|\alpha_Z^-|\Omega'J'(M'=M'')\rangle$ with $\Lambda''=\Omega''=0$ and $\Lambda'=\Omega'=1$.

We can evaluate the matrix elements of α_I^j with the help of Hougen's monograph [42]. Hougen tells us (Table 6, page 31) that these matrix elements are given by a product of three factors:

$$\langle\Omega'J'M'|\alpha_I^j|\Omega JM\rangle = f(J'J)g_j h_I, \tag{8}$$

with each factor taken from the appropriate row of his Table VI. In the case of $\alpha_I^+ = \alpha_I^x + i\alpha_I^y$, corresponding to $\Delta\Omega = -1$, we note that the factor $g_+ = g_x + ig_y = 2g_x$. Similarly, for $\alpha_I^- = \alpha_I^x - i\alpha_I^y$, corresponding to $\Delta\Omega = +1$, the factor $g_- = g_x - ig_y = 2g_x$.

TABLE I. Matrix elements of direction cosine operator components (orientation factors) linking unit vectors in the space fixed (XYZ) and body fixed (xyz) coordinate systems, $\langle(\Omega_u=\Omega+1)J_uM|\alpha_Z^-|\Omega JM\rangle$, for $^1\Pi(v_u,J_u,M) \leftarrow {}^1\Sigma(v,J,M)$ and $^1\Delta(v_u,J_u,M) \leftarrow {}^1\Pi(v,J,M)$ transitions with $\Delta M=0$ (induced by linearly polarized light). The J and M quantum numbers in the expressions below correspond to the lower level of the transition. $\Omega=0$, and 1 for the $^1\Pi \leftarrow {}^1\Sigma$ and $^1\Delta \leftarrow {}^1\Pi$ transitions, respectively.

	$\langle(\Omega_u=\Omega+1)J_uM\|\alpha_Z^-\|\Omega JM\rangle$	
	$^1\Pi(v_u,J_u,M) \leftarrow {}^1\Sigma(v,J,M)$	$^1\Delta(v_u,J_u,M) \leftarrow {}^1\Pi(v,J,M)$
R lines $J_u=J+1$	$-\frac{\sqrt{(J+2)}\sqrt{(J+1)^2-M^2}}{\sqrt{(J+1)}\sqrt{(2J+1)(2J+3)}}$	$-\frac{\sqrt{(J+2)(J+3)}\sqrt{(J+1)^2-M^2}}{(J+1)\sqrt{(2J+1)(2J+3)}}$
Q lines $J_u=J$	$\frac{M}{\sqrt{J(J+1)}}$	$\frac{\sqrt{(J-1)(J+2)}M}{J(J+1)}$
P lines $J_u=J-1$	$\frac{\sqrt{(J-1)}\sqrt{J^2-M^2}}{\sqrt{J}\sqrt{(2J+1)(2J-1)}}$	$\frac{\sqrt{(J-1)(J-2)}\sqrt{J^2-M^2}}{J\sqrt{(2J+1)(2J-1)}}$

Table I provides expressions for the matrix elements of the direction cosine operator components, $\langle(\Omega_u=\Omega+1)J_u(M_u=M)|\alpha_Z^-|\Omega\,J\,M\rangle$ for $^1\Pi \leftarrow {}^1\Sigma$ and $^1\Delta \leftarrow {}^1\Pi$ transitions. Spano [43] refers to these matrix elements as orientation factors, $F^0_{\Lambda\to\Lambda'}(J,M;J',M'=M)$, and presents expressions for them for $^1\Sigma \leftarrow {}^1\Sigma$ and $^1\Pi \leftarrow {}^1\Sigma$ transitions in his Tables I and II, respectively. He also presents expressions for $F^1_{\Lambda\to\Lambda'}(J,M;J',M'=M+1)$ and $F^{-1}_{\Lambda\to\Lambda'}(J,M;J',M'=M-1)$ corresponding to

TABLE II. Predicted (via direction cosine operator matrix elements) and experimentally observed probe line rotational branch signal strength ratios (P:Q:R) for specified J' and J'' double resonance combinations. Note that for each (intermediate state) J' specified below, the corresponding (ground state) J'' values used are $J'+1$, J', $J'-1$ for P, Q, and R pump excitations, respectively.

J'	Pump	Predicted (P:Q:R)	Observed (P:Q:R)
10	R	0.54 : 0.65 : 1	0.65 : 0.73 : 1
	Q	0.11 : 1 : 0.25	0.34 : 1 : 0.52
	P	0.53 : 0.83 : 1	0.80 : 0.97 : 1
3	R	0.11 : 0.26 : 1	0.09 : 0.36 : 1
	Q	0.03 : 1 : 0.55	0.03 : (0.45 : 1)[a]
	P	0.10 : 0.54 : 1	0.30 : 0.66 : 1
2	R	0 : 0.13 : 1	0 : 0.18 : 1
	Q	0 : 1 : 0.94	0 : (0.66 : 1)[a]
	P	0 : 0.38 : 1	0 : 0.40 : 1
1	R	0 : 0 : 1	0 : 0 : 1
	Q	0 : 0 : 1	0 : 0 : 1
	P	0 : 0 : 1	0 : 0 : 1

[a]Inconsistent with prediction—possibly due to additional resonances around the R probe branches, or perturbed upper e parity levels of the Q probe branches.

$\Delta M = +1$ and $\Delta M = -1$ transitions induced by left and right circularly polarized light, respectively. Note that in Spano's tables, the primed values represent the upper level and the unprimed values represent the lower level of the transition. For future reference, in the Supplemental Material [44], we present matrix elements $\langle \Omega' J' M' | \alpha_I^j | \Omega J M \rangle = f(J'J) g_j h_I = F^{\Delta M}_{\Lambda \to \Lambda'}(J, M; J', M')$ for $^1\Sigma \leftarrow {}^1\Sigma$, $^1\Pi \leftarrow {}^1\Pi$, $^1\Delta \leftarrow {}^1\Delta$, $^1\Pi \leftarrow {}^1\Sigma$, $^1\Delta \leftarrow {}^1\Pi$, $^1\Sigma \leftarrow {}^1\Pi$, and $^1\Pi \leftarrow {}^1\Delta$ transitions with $\Delta M = 0, \pm 1$.

Using the expressions in Table I, we can predict ratios of rotational branch intensities for our double resonance excitation spectra using Eq. (7). We find that these are in reasonable agreement with observation when evaluated for $J' = 10$ ($J'' = 9$, 10, 11), $J' = 3$ ($J'' = 2$, 3, 4), $J' = 2$ ($J'' = 1$, 2, 3), and $J' = 1$ ($J'' = 0$, 1, 2). Both the theoretically predicted and the experimentally observed rotational-branch signal strengths for the above-mentioned J', J'' combinations are presented in Table II as fractions of the largest probe branch intensity for a given pump excitation.

Finally, by comparing the molecular constants of the observed $^1\Delta_g$ states with *ab initio* predictions [13], we were able to identify them as the $3^1\Delta_g$ and $4^1\Delta_g$ electronic states originating from the $5s + 5d$ and $5s + 4f$ atomic limits, respectively. We would like to note that triplet states with singlet admixture were ruled out as potential candidates for the observed states based on the lack of well-defined Franck-Condon structures in their bound-free fluorescence [45,46] to the repulsive part of the $a^3\Sigma_u^+$ triplet ground state potential. The absence of the characteristic oscillatory Franck-Condon structures in the resolved bound-free spectra of the LIF (as illustrated in Fig. 4) indicates that the molecules in the two observed excited states do not directly radiate to the $a^3\Sigma_u^+$ state, but instead that the fluorescence is emitted following collisional transfer of population to multiple vibrational levels that exhibit singlet-triplet character mixing. This is in contrast to the bound-free fluorescence from individual levels of triplet states where well defined oscillations determined by the vibrational wave function of the excited state are present, as we have observed, for example, for the $3^3\Pi_g$ and $4^3\Sigma_g^+$ states of the Rb_2 molecule [17].

In addition to the direct probe laser excitation lines, we have observed a number of satellite lines which arise from collisions of excited $B^1\Pi_u$ state Rb_2 molecules with argon or rubidium atoms that are also present in the heat-pipe oven [see Fig. 5(a)]. It is interesting to note that we have observed that the Rb_2 molecules in the intermediate $B^1\Pi_u$ state experience collisions where ΔJ can be even or odd. This contrasts with the case of homonuclear $^1\Sigma$ molecules where only collisions with even ΔJ can be observed [15–17]. The total symmetry (parity) of the molecule must be rigorously preserved during transitions, including transitions arising from collisions. Considering that collisions which change the nuclear spin symmetry are rare [40,47], a propensity for transfer between symmetric-symmetric ($s \leftrightarrow s$) and antisymmetric-antisymmetric ($a \leftrightarrow a$) levels exists [40]. Transfer between symmetric and antisymmetric levels ($s \nleftrightarrow a$) is strongly suppressed. Since each rotational level of a $^1\Pi$ state is split into a symmetric and an antisymmetric component by the Λ-type doubling, even and odd J changing collisions, $\Delta J = \pm 1, \pm 2, \ldots$, are possible as shown in Fig. 5(b). Odd J changing collisions occur between Λ doublet components with the opposite e/f (rotationless) parity while even J changing collisions occur between Λ doublet components of the same e/f parity.

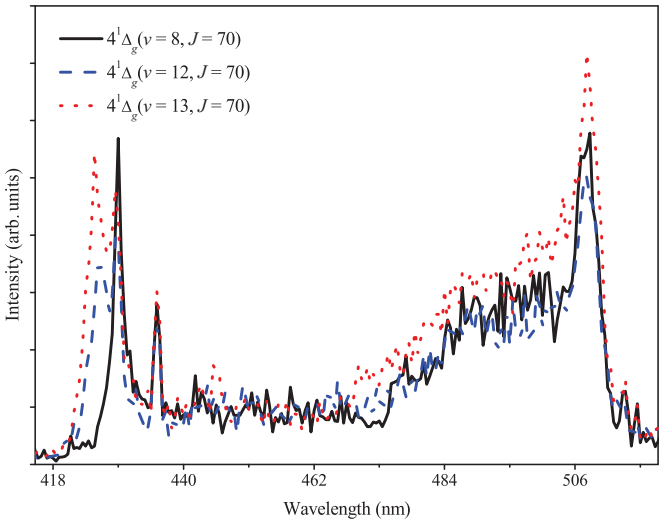

FIG. 4. The resolved bound-free emission to the repulsive region of the $a^3\Sigma_u^+$ state potential following double resonance excitation of several vibrational levels of the $4^1\Delta_g$ electronic state. The spectra lack the characteristic bound-free oscillations observed in the spectra of directly excited triplet states [17]. Furthermore, no significant variations are observed between the spectra originating from different vibrational levels. This indicates that the upper levels of the observed fluorescence are collisionally populated. Very similar behavior of the bound-free fluorescence was also observed in the case of double resonance excitation of the $3^1\Delta_g$ electronic state.

The observed rovibrational energy levels for the $3^1\Delta_g$ and $4^1\Delta_g$ states are shown in Fig. 6 and are also listed in the Supplemental Material at [44]. The rotational assignments of the term values are based on the confirmed intermediate state quantum numbers; i.e., probe excitations involving the $B^1\Pi_u(v', J')$ level will have the automatic assignments of $J_P = J' - 1$, $J_Q = J'$, and $J_R = J' + 1$, where the subscripts denote the observed probe branch. The absence of selection rules for vibrational transitions makes the assignment of the vibrational quantum number intrinsically difficult. Thus, our vibrational assignments are derived from the assumption that $v = 0$ for the lowest observed level for each state. To rule out the existence of lower vibrational levels we have extensively searched, with negative results, the energy range below the lowest observed vibrational level.

After assigning both the rotational and vibrational quantum numbers to the observed energy levels of the $3^1\Delta_g$ and $4^1\Delta_g$ electronic states, the data were least-squares fit to the Dunham expansion [48] given by

$$T_{v,J} = T_e + \sum_{k,l} Y_{k,l} \left(v + \frac{1}{2} \right)^k [J(J+1) - \Lambda^2]^l. \quad (9)$$

An iterative process of deciding whether to include or exclude particular observed level energies where levels appear to be strongly perturbed was executed, in addition to varying the

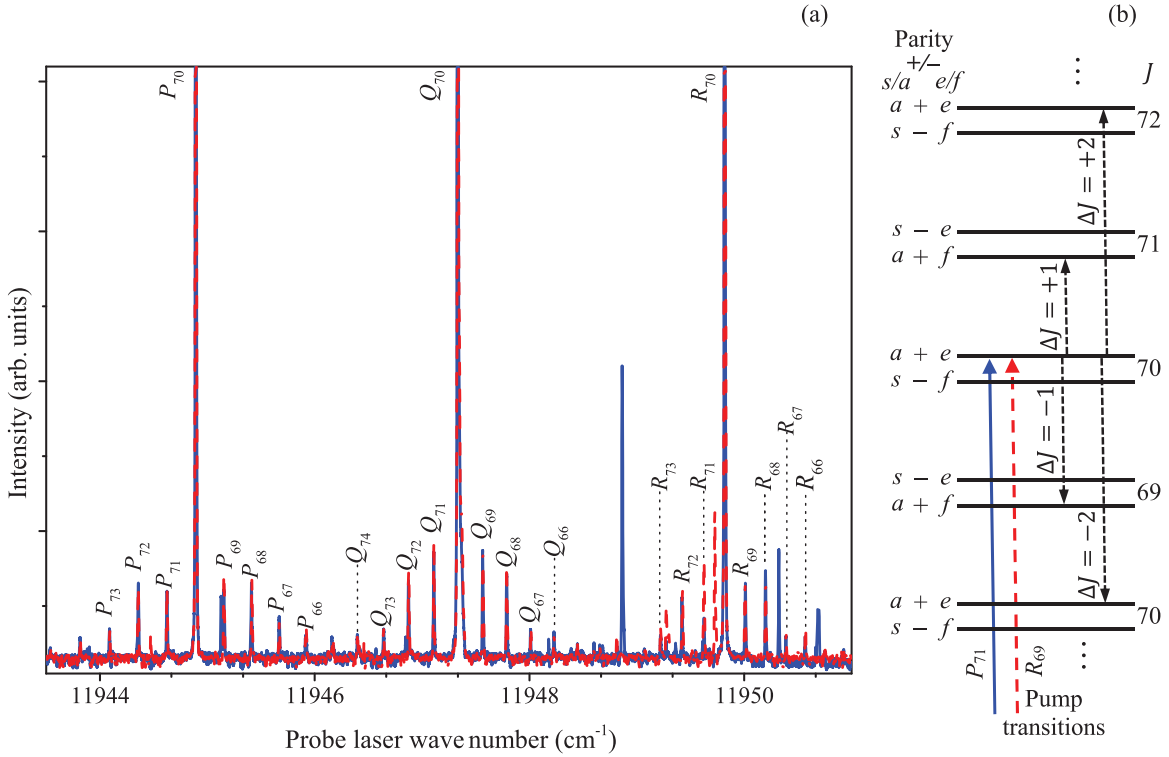

FIG. 5. (a) A probe laser excitation spectrum of the $4^1\Delta_g(v=0)$ vibrational level following pump laser excitation of the $B^1\Pi_u(v'=5,\ J'=70)$ intermediate level. The solid (blue) and dashed (red) trace correspond to pump laser P_{71} and R_{69} branch excitations to the intermediate level from the $X^1\Sigma_g^+(v''=0)$ ground state vibrational level, respectively. In addition to the main (parent) P_{70}, Q_{70}, and R_{70} lines, satellite lines originating from collision-induced even and odd ΔJ rotational energy transfer in the intermediate level are observed. (b) Schematic illustration of the rotational energy transfer originating from the $B^1\Pi_u(v'=5,\ J'=70)$ intermediate level. The even and odd J-changing collisions are given with black dashed arrows while the P_{71} and R_{69} pump laser excitations populating the $B^1\Pi_u(v'=5,\ J'=70)$ intermediate level are given with solid blue and red dashed arrows.

number of computed Dunham constants to optimize the set of molecular constants for each electronic state. All data points were given equal weight in the fitting process since all data were collected under the same experimental conditions. The final results of the fitting process for both states are given in Table III. The residuals for each fitted level are illustrated in Fig. 7. In Table IV the traditional molecular constants T_e, $\omega_e \approx Y_{10}$, and $B_e \approx Y_{01}$ of the states are compared with *ab initio* results [13,49]. The T_e constant is calculated by subtracting from the $T_e + Y_{00}$ fit result of Eq. (9) the value of Y_{00}, estimated using the expression [48]

$$Y_{00} \cong \frac{Y_{01}+Y_{20}}{4} - \frac{Y_{11}Y_{10}}{12Y_{01}} + \frac{Y_{11}^2 Y_{10}^2}{144Y_{01}^3}. \tag{10}$$

The Y_{00} values for the $3^1\Delta_g$ and $4^1\Delta_g$ states are -3.66×10^{-1} cm^{-1} and -1.08×10^{-1} cm^{-1}, respectively.

TABLE III. Dunham expansion coefficients (in cm^{-1}) of the $3^1\Delta_g$ and $4^1\Delta_g$ electronic states of $^{85}Rb_2$ obtained by a direct fit of the experimental data. Note that additional digits, beyond what are statistically significant, are given to avoid rounding errors. Uncertainties in the final digits are given in parentheses.

$k,\ l$	Y_{kl} for $3^1\Delta_g$	Y_{kl} for $4^1\Delta_g$
$T_e + Y_{00}$	26 710.37 (51)	26 853.16 (30)
Y_{10}	51.982 (366)	48.638 (379)
Y_{20}	−2.5258 (1088)	$-5.0470\ (14940)\times10^{-1}$
Y_{30}	$2.5976\ (1396)\times10^{-1}$	$-6.5968\ (23776)\times10^{-2}$
Y_{40}	$-1.2775\ (775)\times10^{-2}$	$-4.7777\ (16312)\times10^{-3}$
Y_{50}	$2.2581\ (1534)\times10^{-4}$	$1.1919\ (4020)\times10^{-4}$
Y_{01}	$1.8255\ (79)\times10^{-2}$	$1.7509\ (47)\times10^{-2}$
Y_{11}	$-2.548\ (232)\times10^{-4}$	$-3.985\ (532)\times10^{-5}$
Y_{21}	$7.49\ (125)\times10^{-6}$	

TABLE IV. Comparisons of the experimental molecular constants of the $3^1\Delta_g$ and $4^1\Delta_g$ states with theoretical predictions. All values reported are in cm^{-1} units.

State	T_e	ω_e	B_e	Ref.
	26 710.74	51.982	0.0182 55	this paper
$3^1\Delta_g$	26 697.7	47.4	0.018 09	[13]
	27 212	56.5	0.016 68[a]	[49]
$4^1\Delta_g$	26853.27	48.638	0.0175 09	this paper
	26 886.7	43.2	0.016 96	[13]

[a]Calculated from the listed R_e value using the expression $B_e = \frac{h\times10^{-2}}{8\pi^2\mu c}\times\frac{1}{R_e^2}$, where B_e is in cm^{-1} units while all physical constants are in SI units [39].

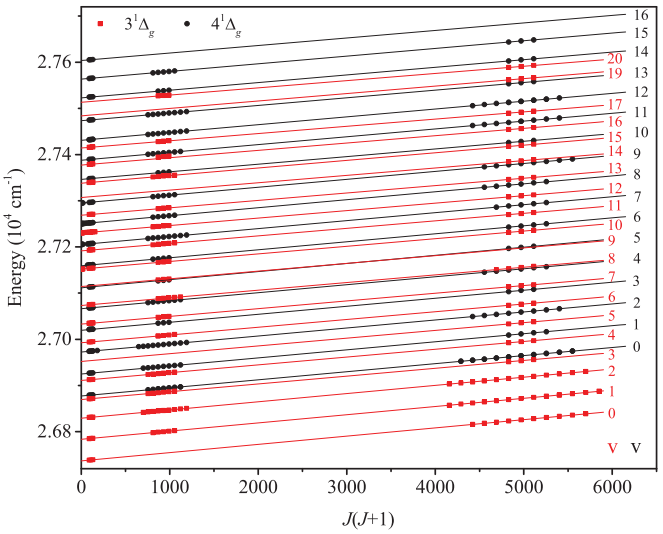

FIG. 6. Assigned rovibrational levels of the $3^1\Delta_g$ and $4^1\Delta_g$ electronic states. 480 rovibrational levels spanning from $v = 0$ to $v = 20$ and $J = 2$ to $J = 74$ were assigned for the $3^1\Delta_g$ state, and 543 rovibrational levels spanning from $v = 0$ to $v = 16$ and $J = 2$ to $J = 76$ were assigned for the $4^1\Delta_g$ state.

From the final set of Dunham constants the potential-energy curve of each state was generated with the computer program RKR1 [50] by implementing the semiclassical Rydberg-Klein-Rees (RKR) method [51–54]. The RKR calculations include the Kaiser correction [55,56], which consists of adding the constant Y_{00} to the vibrational energy and changing $v_{\min}$ in the f and g integrals from $-1/2$ to the value that satisfies the equation $Y_{00} + G(v) = 0$. The resulting turning points, $R_{\min}$ and $R_{\max}$, along with the corresponding values of the potential-energy functions relative to their minima, $G_v + Y_{00} = \sum_k Y_{k,0}(v + \frac{1}{2})^k$, are given in Tables V and VI for the $3^1\Delta_g$ and $4^1\Delta_g$ states, respectively. The tables also include the effective value of v associated with the potential minimum of each state ($v_{\min} = -0.4930$ for the $3^1\Delta_g$ state and $v_{\min} = -0.4978$ for the $4^1\Delta_g$ state). In Fig. 8 the RKR curves are compared with *ab initio* potential-energy curves from Ref. [13].

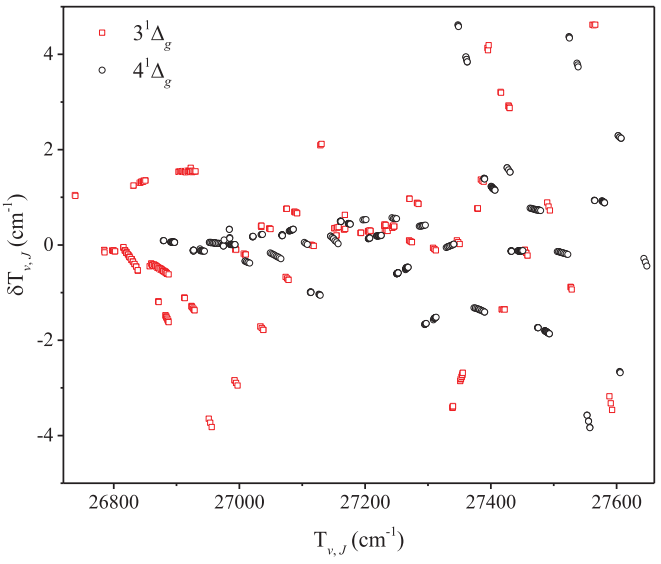

FIG. 7. Residuals (observed energies minus energies calculated from the fitted Dunham coefficients) for the $3^1\Delta_g$ (red squares) and $4^1\Delta_g$ (black circles) states of the $^{85}Rb_2$ molecule.

TABLE V. RKR potential of the $^{85}Rb_2$ $3^1\Delta_g$ state generated from the Dunham coefficients listed in Table III.

v	$R_{\min}$ (Å)	$R_{\max}$ (Å)	$G_v + Y_{00}$ (cm^{-1})
−0.4930	$R_e = 4.664009$		0
0	4.551179	4.801427	25.025
1	4.476051	4.926103	72.737
2	4.427167	5.023714	117.383
3	4.389453	5.108893	159.967
4	4.358807	5.185375	201.252
5	4.333243	5.254890	241.791
6	4.311430	5.318631	281.951
7	4.292300	5.377627	321.942
8	4.274944	5.432827	361.845
9	4.258572	5.485098	401.635
10	4.242508	5.535216	441.212
11	4.226190	5.583842	480.427
12	4.209681	5.632015	519.109
13	4.193052	5.680492	557.091
14	4.176366	5.729678	594.239
15	4.159665	5.779519	630.478
16	4.142953	5.829369	665.820
17	4.126179	5.877831	700.388
18	4.109217	5.922629	734.449
19	4.091839	5.960586	768.434
20	4.073690	5.987811	802.972

TABLE VI. RKR potential of the $^{85}Rb_2$ $4^1\Delta_g$ state generated from the Dunham coefficients listed in Table III.

v	$R_{\min}$ (Å)	$R_{\max}$ (Å)	$G_v + Y_{00}$ (cm^{-1})
−0.4978	$R_e = 4.762092$		0
0	4.637608	4.893615	24.093
1	4.549339	4.996156	71.914
2	4.490204	5.069673	119.190
3	4.443290	5.131024	166.118
4	4.403631	5.185149	212.817
5	4.368876	5.234403	259.340
6	4.337644	5.280182	305.689
7	4.309032	5.323419	351.833
8	4.282408	5.364777	397.715
9	4.257330	5.404727	443.275
10	4.233498	5.443586	488.457
11	4.210736	5.481527	533.227
12	4.188984	5.518582	577.586
13	4.168295	5.554624	621.587
14	4.148839	5.589367	665.345
15	4.130896	5.622356	709.052
16	4.114850	5.652973	752.998

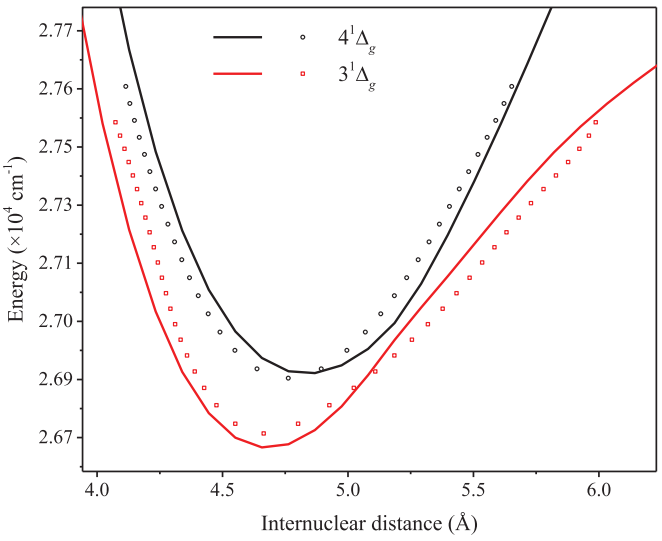

FIG. 8. Potential-energy curves for the $3^1\Delta_g$ and $4^1\Delta_g$ electronic states of $^{85}Rb_2$. The *ab initio* calculations of Ref. [13] are plotted with solid lines while the RKR generated results from our optimized sets of Dunham parameters are presented with red squares and black circles for the $3^1\Delta_g$ and $4^1\Delta_g$ states, respectively.

IV. CONCLUSIONS

Our experimental results for the $3^1\Delta_g$ state are in very close agreement with the *ab initio* results of Ref. [13] with a difference in potential well energy minimum of less than 13 cm^{-1}. The well minimum for the $4^1\Delta_g$ state is also in fairly good agreement with *ab initio* calculations [13] but differs by about 33 cm^{-1}. Reference [13] predicts ~ 5 cm^{-1} smaller vibrational spacing for both $^1\Delta_g$ states than what we observe. In addition, the experimentally derived rotational constant B_e for both states follow the *ab initio* predictions closely. From the residuals of the Dunham fits plotted in Fig. 7 we can infer that strong perturbations are present throughout the entire observed range of the $3^1\Delta_g$ state while in the case of the $4^1\Delta_g$ state the perturbations are prevalent only above 27260 cm^{-1}. This indicates that the $3^1\Delta_g$ state is globally perturbed by an unobserved state and that these perturbations also most likely involve the $4^1\Delta_g$ levels above the avoided crossing region of the two states at ~ 5.2 Å.

In summary, the present work reports the experimental study of the $3^1\Delta_g$ and $4^1\Delta_g$ states of Rb_2. We have observed a large set of rovibrational levels from these states using the OODR technique. A Dunham fit to our data provides the desired molecular constants which are then used to construct RKR potential-energy curves. Our results are in good agreement with the latest *ab initio* calculations [13].

ACKNOWLEDGMENTS

This work was supported by the National Science Foundation (Grants No. PHY 1912269, No. PHY 2018443, and No. PHY 2207665) and the Lagerqvist Research Fund of Temple University.

[1] A. Kramida, Y. Ralchenko, and J. Reader, NIST ASD Team, *NIST Atomic Spectra Database (ver. 5.6.1), [Online]* (National Institute of Standards and Technology, Gaithersburg, MD, 2018).

[2] K. K. Ni, S. Ospelkaus, M. H. G. de Miranda, A. Pe'er, B. Neyenhuis, J. J. Zirbel, S. Kotochigova, P. S. Julienne, D. S. Jin, and J. Ye, A high phase-space-density gas of polar molecules, Science **322**, 231 (2008).

[3] J. G. Danzl, E. Haller, M. Gustavsson, M. J. Mark, R. Hart, N. Bouloufa, O. Dulieu, H. Ritsch, and H.-C. Naegerl, Quantum gas of deeply bound ground state molecules, Science **321**, 1062 (2008).

[4] M. H. G. de Miranda, A. Chotia, B. Neyenhuis, D. Wang, G. Quemener, S. Ospelkaus, J. L. Bohn, J. Ye, and D. S. Jin, Controlling the quantum stereodynamics of ultracold bimolecular reactions, Nat. Phys. **7**, 502 (2011).

[5] B. Yan, S. A. Moses, B. Gadway, J. P. Covey, K. R. A. Hazzard, A. M. Rey, D. S. Jin, and J. Ye, Observation of dipolar spin-exchange interactions with lattice-confined polar molecules, Nature (London) **501**, 521 (2013).

[6] T. M. Rvachov, H. Son, A. T. Sommer, S. Ebadi, J. J. Park, M. W. Zwierlein, W. Ketterle, and A. O. Jamison, Long-lived ultracold molecules with electric and magnetic dipole moments, Phys. Rev. Lett. **119**, 143001 (2017).

[7] C. Gross and I. Bloch, Quantum simulations with ultracold atoms in optical lattices, Science **357**, 995 (2017).

[8] X. D. He, K. P. Wang, J. Zhuang, P. Xu, X. Gao, R. J. Guo, C. Sheng, M. Liu, J. Wang, J. M. Li, G. V. Shlyapnikov, and M. S. Zhan, Coherently forming a single molecule in an optical trap, Science **370**, 331 (2020).

[9] W. B. Cairncross, J. T. Zhang, L. R. B. Picard, Y. C. Yu, K. Wang, and K. K. Ni, Assembly of a rovibrational ground state molecule in an optical tweezer, Phys. Rev. Lett. **126**, 123402 (2021).

[10] J. J. Park, Y. K. Lu, A. O. Jamison, T. V. Tscherbul, and W. Ketterle, A Feshbach resonance in collisions between triplet ground-state molecules, Nature (London) **614**, 54 (2023).

[11] A. Pashov, P. Kowalczyk, A. Grochola, J. Szczepkowski, and W. Jastrzebski, Coupled-channels analysis of the ($5^1\,\Sigma_u^+$, $5^1\,\Pi_u$, $5^3\,\Pi_u$, $2^3\Delta_u$) complex of electronic states in rubidium dimer, J. Quant. Spectrosc. Radiat. Transfer **221**, 225 (2018).

[12] W. Jastrzebski, A. Grochola, J. Szczepkowski, and P. Kowalczyk, Polarisation labelling spectroscopy of rubidium dimer: Highly excited $8^1\Sigma_u^+$, $9^1\Sigma_u^+$ and $8^1\Pi_u$ states, J. Mol. Struct. **1208**, 127858 (2020).

[13] W. Jastrzebski, P. Kowalczyk, J. Szczepkowski, A. R. Allouche, P. Crozet, and A. J. Ross, High-lying electronic states of the rubidium dimer – *Ab initio* predictions and experimental observation of the $5^1\Sigma_u^+$ and $5^1\Pi_u$ states of Rb_2 by polarization labelling spectroscopy, J. Chem. Phys. **143**, 044308 (2015).

[14] Y. Lee, S. Lee, and B. Kim, Mass-resolved resonance enhanced ionization study of complicated excited electronic states of Rb_2 near 430 nm and their predissociation dynamics, J. Phys. Chem. A **111**, 11750 (2007).

[15] P. T. Arndt, V. B. Sovkov, J. Ma, X. H. Pan, D. S. Beecher, J. Y. Tsai, Y. F. Guan, A. M. Lyyra, and E. H. Ahmed, The Rb_2 $3^1\Pi_g$ state: Observation and analysis, J. Chem. Phys. **149**, 224303 (2018).

[16] P. T. Arndt, V. B. Sovkov, J. Ma, X. H. Pan, D. S. Beecher, J. Y. Tsai, Y. F. Guan, A. M. Lyyra, and E. H. Ahmed, Experimental study of the $6^1\Sigma_g^+$ state of the rubidium dimer, Phys. Rev. A **99**, 052511 (2019).

[17] P. T. Arndt, V. B. Sovkov, J. Ma, X. Pan, D. S. Beecher, J. Y. Tsai, R. Livingston, V. M. Marcune, A. M. Lyyra, and E. H. Ahmed, Experimental study of the $3^3\Pi_g$ and $4^3\Sigma_g^+$ states of the rubidium dimer, Phys. Rev. A **105**, 032823 (2022).

[18] L. Li and R. W. Field, Direct observation of high-lying $^3\Pi_g$ states of the sodium molecule by optical-optical double resonance, J. Phys. Chem. **87**, 3020 (1983).

[19] R. A. Bernheim, L. P. Gold, and T. Tipton, Rydberg states of $^7Li_2$ by pulsed optical–optical double resonance spectroscopy: Molecular constants of $^7Li_2^+$, J. Chem. Phys. **78**, 3635 (1983).

[20] X. B. Xie and R. W. Field, Perturbation facilitated optical-optical double resonance spectroscopy of the $^6Li_2$ $3^3\Sigma_g^+$, $2^3\Pi_g$, $1^3\Delta_g$, $b^3\Pi_u$, and $a^3\Sigma_u^+$ state, J. Mol. Spectrosc. **117**, 228 (1986).

[21] J. R. de Laeter, J. K. Böhlke, P. De Biévre, H. Hidaka, H. S. Peiser, K. J. R. Rosman, and P. D. P. Taylor, Atomic weights of the elements. Review 2000 (IUPAC technical report), Pure Appl. Chem. **75**, 683 (2003).

[22] C. R. Vidal and J. Cooper, Heat-pipe oven: A new, well-defined metal vapor device for spectroscopic measurements, J. Appl. Phys. **40**, 3370 (1969).

[23] A. N. Nesmeyanov, *Vapor Pressure of the Chemical Elements* (Elsevier, Amsterdam, 1963).

[24] T. W. Hänsch, K. C. Harvey, G. Meisel, and A. L. Schawlow, Two-photon spectroscopy of Na 3s-4d without Doppler broadening using a cw dye laser, Opt. Commun. **11**, 50 (1974).

[25] F. Biraben, B. Cagnac, and G. Grynberg, Experimental evidence of 2-photon transition without doppler broadening, Phys. Rev. Lett. **32**, 643 (1974).

[26] R. Salomaa and S. Stenholm, 2-photon spectroscopy - effects of a resonant intermediate state, J. Phys. B **8**, 1795 (1975).

[27] E. Ahmed and A. M. Lyyra, Effect of Doppler broadening on Autler-Townes splitting in the molecular cascade excitation scheme, Phys. Rev. A **76**, 053407 (2007).

[28] E. H. Ahmed, J. Huennekens, T. Kirova, J. B. Qi, and A. M. Lyyra, The Autler-Townes effect in molecules: Observations, theory, and applications, in *Advances in Atomic, Molecular, and Optical Physics*, edited by E. Arimondo, P. R. Berman, and C. C. Lin (Elsevier, Amsterdam, 2012), Vol. 61, p. 467–514.

[29] J. Y. Seto, R. J. Le Roy, J. Verges, and C. Amiot, Direct potential fit analysis of the $X\,^1\Sigma_g^+$ state of Rb_2: Nothing else will do!, J. Chem. Phys. **113**, 3067 (2000).

[30] C. Amiot and J. Vergès, Optical-optical double resonance and Fourier transform spectroscopy: The Rb_2 $B^1\Pi_u$ electronic state up to the quasibound energy levels, Chem. Phys. Lett. **274**, 91 (1997).

[31] S. Gerstenkorn and P. Luc, *Atlas of the Absorption Spectra of Molecular Iodine for* 14, 800 cm^{-1} *to* 20, 000 cm^{-1} (CNRS, Paris, 1978).

[32] S. Gerstenkorn and P. Luc, Absolute iodine I_2 standards measured by means of Fourier-transform spectroscopy, Rev. Phys. Appl. **14**, 791 (1979).

[33] R. A. Keller, R. Engleman, and B. A. Palmer, Atlas for optogalvanic wavelength calibration, Appl. Opt. **19**, 836 (1980).

[34] B. A. Palmer, R. A. Keller, and R. Engleman, *An Atlas of Uranium Emission Intensities in a Hollow Cathode Discharge* (Los Alamos Scientific Laboratory, New Mexico, 1980).

[35] L. Li, Q. S. Zhu, A. M. Lyyra, T. J. Whang, W. C. Stwalley, R. W. Field, and M. H. Alexander, Collision-induced transitions between $A^1\Sigma_u^+$ and $b\,^3\Pi_u$ states of Na_2 - the gateway effect of perturbed levels, J. Chem. Phys. **97**, 8835 (1992).

[36] L. Li, S. Antonova, A. Yiannopoulou, K. Urbanski, and A. M. Lyyra, State-to-state collision energy transfer of $^7Li_2$ within high-lying triplet states: Gateway effect of mixed levels in energy transfer between singlet and triplet states, J. Chem. Phys. **105**, 9859 (1996).

[37] E. H. Ahmed, X. Pan, J. Huennekens, and A. M. Lyyra, Optical control of collisional population flow between molecular electronic states of different spin multiplicity, Phys. Rev. A **89**, 061401(R) (2014).

[38] B. Beser, V. B. Sovkov, J. Bai, E. H. Ahmed, C. C. Tsai, F. Xie, L. Li, V. S. Ivanov, and A. M. Lyyra, Experimental investigation of the $^{85}Rb_2$ $a\,^3\Sigma_u^+$ triplet ground state: Multiparameter Morse long range potential analysis, J. Chem. Phys. **131**, 094505 (2009).

[39] P. F. Bernath, *Spectra of Atoms and Molecules*, 2nd ed. (Oxford University Press, New York, 2005).

[40] G. Herzberg, *Spectra of Diatomic Molecules* (Van Nostrand, New York, 1950).

[41] H. Lefebvre-Brion and R. W. Field, *The Spectra and Dynamics of Diatomic Molecules* (Academic, Amsterdam, 2004).

[42] J. T. Hougen, The Calculation of Rotational Energy Levels and Rotational Line Intensities in Diatomic Molecules, NBS Monogr. (US) **115** (1970).

[43] F. C. Spano, Theory of sub-Doppler Autler-Townes splitting in molecules: Alignment and orientation of the angular momentum in nonpolar molecules, J. Chem. Phys. **114**, 276 (2001).

[44] See Supplemental Material at http://link.aps.org/supplemental/10.1103/PhysRevA.109.012805 for the experimental term values and the matrix elements of direction cosine operator components for common molecular transitions.

[45] E. J. Breford and F. Engelke, Laser-induced molecular fluorescence in supersonic nozzle beams: Applications to the NaK $D^1\Pi$ - $X^1\Sigma^+$ and $D^1\Pi$ - $a^3\Sigma^+$ systems, Chem. Phys. Lett. **53**, 282 (1978).

[46] E. U. Condon, Nuclear motions associated with electron transitions in diatomic molecules, Phys. Rev. **32**, 858 (1928).

[47] C. Ottinger, R. Velasco, and R. N. Zare, Some propensity rules in collision-induced rotational quantum jumps, J. Chem. Phys. **52**, 1636 (1970).

[48] J. L. Dunham, The energy levels of a rotating vibrator, Phys. Rev. **41**, 721 (1932).

[49] M. Tomza, W. Skomorowski, M. Musial, R. Gonzalez-Ferez, C. P. Koch, and R. Moszynski, Interatomic potentials, electric properties and spectroscopy of the ground and excited states of the Rb_2 molecule: Ab initio calculations and effect of a non-resonant field, Mol. Phys. **111**, 1781 (2013).

[50] R. J. Le Roy, RKR1: A computer program implementing the first-order RKR method for determining diatomic molecule

potential energy functions, J. Quantitative Spectroscopy & Radiative Transfer **186**, 158 (2017).

[51] R. Rydberg, Graphical representation of some bound spectroscopic results, Z. Phys. **73**, 376 (1932).

[52] R. Rydberg, Some potential curves of mercury hydrides, Z. Phys. **80**, 514 (1933).

[53] O. Klein, For the calculation of potential curves for diatomic molecules with spectral help, Z. Phys. **76**, 226 (1932).

[54] A. L. G. Rees, The calculation of potential-energy curves from band-spectroscopic data, Proc. Phys. Soc. London **59**, 998 (1947).

[55] E. W. Kaiser, Dipole moment and hyperfine parameters of $H^{35}Cl$ and $D^{35}Cl$, J. Chem. Phys. **53**, 1686 (1970).

[56] J. Tellinghuisen, A direct potential fitting RKR method: Semiclassical vs. quantal comparisons, J. Mol. Spectrosc. **330**, 20 (2016).